

Correlation of shear forces and heat conductance in nanoscale junctionsBenjamin J. Robinson ^{1,2}, Manuel E. Pumarol,¹ and Oleg V. Kolosov ^{1,2,*}¹*Physics Department, Lancaster University, Lancaster LA1 4YB, United Kingdom*²*Materials Science Institute, Lancaster University, Lancaster LA1 4YW, United Kingdom*

(Received 9 January 2019; revised manuscript received 23 July 2019; published 16 December 2019)

Nanoscale solid-solid contacts are key elements which determine the electrical and thermal behavior of modern electronic devices and micro- and nanoelectromechanical systems. Here we show that simultaneous measurements of the shear force and the heat flow in nanoscale junctions reveal a linear correlation between thermal conductance and maximal shear force, confirming the ballistic nature of heat transport in the junction. Furthermore, we find that here the shear strength and thermal conductance in nanoscale contacts for materials where heat transport is phonon dominated can be linked via the fundamental material properties of heat capacity and group velocity of the heat carriers.

DOI: [10.1103/PhysRevB.100.235426](https://doi.org/10.1103/PhysRevB.100.235426)**I. INTRODUCTION**

As continuously decreasing length scales are exploited in the fundamental architecture of electronic, nanoelectromechanical [1], and nanostructured thermal management devices [2], the nature of nanoscale contacts between solid surfaces and interfaces is becoming increasingly important for understanding many of the properties of these devices. While electron transport [3] and force interaction [4] in such contacts have been well explored, the study of nanoscale heat transport in both active (heat generating) and passive (heat dissipating) nanostructures [5] still poses significant challenges [6] as the critical dimensions of these devices are typically below the mean free path (MFP) of electrons and phonons, the two major types of heat carriers in solid state devices [7].

One of the most versatile approaches for nanoscale thermal mapping is scanning thermal microscopy (SThM) [8]. SThM is a modified atomic force microscopy (AFM) system, which measures the heat transfer through a nanometer dimension contact between the apex of a heated thermal probe [9,10] and the sample of interest, enabling determination of local sample thermal conductivity [11,12] and heat transport down to single quantum accuracy [13,14]. Unfortunately, the generally irregular and fluctuating morphology of the nanoscale solid-solid contact significantly reduces the reliability and effectiveness of these measurements [15].

A tempting approach to resolve this is to perform correlated measurements of the heat transfer and a complementary parameter which is also sensitive to the contact state of the nanoscale junction. For example, recent studies of the heat and electron transport in metallic junctions [13,14] confirmed the Wiedemann-Franz law [16], validating the proportionality of thermal and electrical conductance in metals down to the atomic scale. Thermal transport in a nanoscale junctions was shown to change normal forces [17]; however, in that study the contact area, the physical value that ultimately defines

the contact, was only indirectly determined via the generally unknown tip shape [Fig. 1(a)].

Here we have used a different physical parameter that is both easily measurable in a SThM and also known to be directly dependent on the junction area, namely, the maximal shear (friction) force F_{ms} the junction can support. F_{ms} has been shown, by nanotribology studies elsewhere [18–21], to be directly proportional to the solid-solid contact area of the junction. In our experiments, we measure this shear force via lateral dithering of the sample perpendicular to the long axis of the cantilever while measuring F_{ms} . We then used a change in a normal force, F_n , during an approach and retract cycle of the tip to the surface, at a rate much slower than the dithering frequency, to modulate the contact area. During contact modulation both the change in F_{ms} (or “shear response”) and the heat conductance of the junction were concurrently measured in the same SThM setup (see details in the Supplemental Material (SM) [22]). Unlike comparisons of electrical and thermal transport [13,14], both shear force and heat flow are present for any metallic, semiconductor or insulating contact and could provide a universal platform for exploring fundamental heat transport phenomena in any solid-solid nanoscale junction. Here we have shown the feasibility of this approach for a selection of materials with radically different thermal and electrical properties: insulating quartz and metallic gold are briefly reported (a more comprehensive study of electron heat transport dominated metals is planned) while a phonon heat transport dominated semiconductor (Si) is explored in more depth in this paper.

II. EXPERIMENTAL RESULTS

Correlation of nanoscale thermal and shear responses. In our experiments we used Joule self-heated micro-fabricated SThM resistive probes with either a silicon nitride probe with Pd integrated heater (SP) (Kelvin Nanotechnologies, UK) or a Si probe with doped heater (DS) (AN-200, Anasys Instruments). Experiments were performed in either ambient or high vacuum (HV) 1×10^{-7} mbar environments. The change

*o.kolosov@lancaster.ac.uk

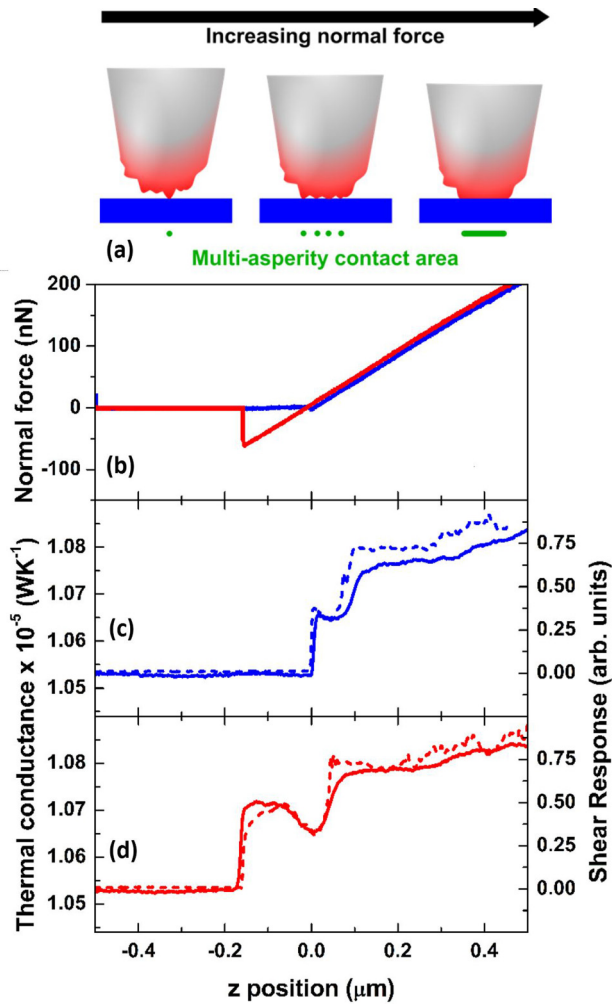


FIG. 1. (a) Schematic of multiasperity contact between a heated SThM probe and sample highlighting the fluctuating nature of the probe-sample nanoscale interface. Simultaneously measured normal force acting at the cantilever (b), and total thermal conductance of the probe $G_t = 1/R_t$ (solid lines) and maximal lateral force (dashed lines) obtained during tip approach to (c) and retracting from (d) the surface.

of probe heater electrical resistance, included in a sensitive Wheatstone bridge circuit (the “thermal response”), is proportional to probe temperature: for a constant power applied to a probe, it is a linear function of the probe temperature and hence probe total thermal resistance R_t or the inverse of it, total thermal conductance $G_t = 1/R_t$; the values most often measured in SThM experiments [8]. In the absence of tip-surface contact, the probe thermal resistance in vacuum, R_p , is defined solely by the heat flowing to the base of the probe, and in ambient environment also by the heat flowing into the air. As the apex of the probe contacts the sample, an additional heat channel with resistance R_j is opened carrying heat to the sample, resulting in decrease of the probe total thermal resistance R_t to R_c . By measuring R_p and R_c one can easily find the tip-surface junction thermal resistance R_j noting that in-contact R_p and R_j are connected in parallel [23,24],

$$R_j = \frac{R_p \times R_c}{R_p - R_c}, \quad (1)$$

and, correspondingly, one can find the total thermal conductance of the junction, $G_j = 1/R_j$ [25].

In our experiments the probe thermal conductance was measured simultaneously with the normal and shear forces during tip-surface approach [typical ambient dependencies are given in supporting materials and HV dependencies in Figs. 1(c) and 1(d)]. The lateral force (shear) response of the probe was recorded at oscillation amplitudes exceeding the sliding threshold at the dithering frequency of 70 Hz; well below cantilever resonances. The lateral AFM signal detected by a lock-in amplifier (“shear response”) was then directly proportional to the maximal shear force in the junction, F_{ms} , and showed no change due to the application of dithering nor any notable oscillation at the dithering frequency. The high torsional stiffness of the SThM probe ensured a negligible tilt of the probe tip, estimated at 2×10^{-5} rad, during dithering. Assuming a contact size of a few nm, this tilt resulted in a variation of the tip-surface distance across the junction below 10^{-13} nm ($\sim 10^{-3}$ of interatomic distance) with no effect on the heat flow in the junction. The shear and thermal responses were recorded as the probe was gradually (10 nm s^{-1}) brought into and out of contact with the sample in the standard force spectroscopy way [26].

Initial studies were performed in ambient conditions on a 100 nm Au-coated polished quartz substrate. In all cases we observed that both thermal and shear responses had a strong variation as the tip was approached and retracted from the sample, with shear response particularly rich in features. Remarkably, in all cases, the behavior of the thermal resistance R_c and shear response was clearly opposite, supported by the correlation analysis of these curves. The correlation coefficient between them was in the range of -1 to -0.8 , well above the level of ± 0.15 for the typical shear force and probe thermal response correlated with simulated noise. Reproducibility of the anticorrelation relationship between shear and thermal response has been confirmed across a wide range of samples: gold (metal with thermal conductivity, k , of $\sim 310 \text{ W m}^{-1} \text{ K}^{-1}$) silicon (semiconductor with $k \sim 149 \text{ W m}^{-1} \text{ K}^{-1}$) and quartz (insulator with $k \sim 1\text{--}10 \text{ W m}^{-1} \text{ K}^{-1}$). This relationship was observed for both the Si (DS) and Si_3N_4 (SP) tipped probes we used (see SM for data on different contact pairs [22]).

Initial, ambient, studies also indicated the presence of fine features observable in both the thermal contact fluctuations and in the shear force; such features are practically absent in the normal force response. However, quantitative heat transport analysis in SThM in ambient conditions is challenging as the probe temperature depends on multiple heat transfer pathways, each with its own associated thermal resistance: (i) solid-solid contact of the probe apex and the sample [27], (ii) through-air heat conduction [28], (iii) heat transfer via water meniscus [29], and (iv) radiative far-field and near-field heat transfer, although the latter has been shown to be generally insignificant in typical SThM measurement conditions [8]. To investigate the relative importance of the heat transfer pathways (i)–(iii) and therefore single out the nanoscale heat transfer phenomena at the tip-sample nanoscale junction, we conducted detailed comparative SThM studies in air and HV environments. Here a DS Si probe was brought into contact with a polished Si surface [Figs. 1(b)–1(d)] while normal

force, thermal response, and shear response were monitored during approach-retract cycles. In order to quantify the link between thermal and shear force phenomena, we compare the shear response with the thermal conductance of the probe-surface junction, G_j .

A gradual change of the probe temperature, as the tip approached the sample surface, was also clearly observed in air (see SM [22]). Such change is associated with conduction of heat from the cantilever to the sample surface via the air; this is fully eliminated in the HV environment [Figs. 1(c) and 1(d)]. Furthermore, as expected, there was significantly greater adhesion in air due to the presence of the tip-sample water bridge, eliminated in HV conditions of 10^{-7} torr; pull-off forces of ~ 137 nN and ~ 62 nN in air and in vacuum, respectively, were measured. The comparison of in-air and in-vacuum measurements (see SM Fig. S4 [22]) estimated the vacuum snap-in junction conductance at 65% of the in-air values, suggesting that solid-solid contact is a dominant heat conductance channel in our Si probe contacts, with water meniscus playing a secondary role. In Fig. 1, we further observe that while an increase of normal forces produces a general rise of the probe thermal conductance G_j , the shear response shows a much more clear correlation with the fluctuating thermal conductance, a feature analyzed in detail below.

III. DISCUSSION

For the simplest case of a single asperity solid-solid contact, one can find the relation between the force acting on the tip, observed as cantilever deflection [26], and the true probe-sample contact radius, a , using the Johnson-Kendal-Roberts (JKR) model, this assumes that surface forces are short range in comparison to the elastic deformations they cause [30,31]. This model is applicable here due to the relatively large adhesion forces and large tip radii and was shown to explain well the elastic contact between the similar AFM tip and the Si surface [32]. As we do not know the radius of curvature of contact, r , we will perform the simulations for the range of the radii of curvature producing the dependence of the maximal shear force F_{ms} and junction thermal conductance G_j for variable loads, and compare these with the experiment.

According to the JKR model, the variation of contact area with normal force equivalent load (L) is given by

$$\frac{a}{a_0} = \left[\frac{1 + \sqrt{1 - L/L_c}}{2} \right]^{\frac{2}{3}}, \quad (2)$$

where L_c is the negative critical load measured in the experiment and load L is directly measured from the deflection of the cantilever using Hooke's law in the standard way [26]. a_0 can then be experimentally determined via the pull-off force of the probe from the sample with a_0 being the contact radius at zero load such that

$$a_0(r) = \left[\frac{6\pi\gamma r^2}{K} \right]^{\frac{1}{3}}, \quad (3)$$

where γ is interfacial energy per unit area (work of adhesion) and K is the effective elastic modulus of tip and sample such that $K = \frac{4}{3} \left[\frac{1-\nu_1^2}{E_1} + \frac{1-\nu_2^2}{E_2} \right]$, where E_1 and E_2 are the Young's

moduli of tip and sample, respectively, and ν_1, ν_2 are Poisson's ratios of the tip and sample, respectively. Here $E_{Si} = 160$ GPa and $\nu_{Si} = 0.27$.

The surface energy γ can then be directly determined from the experimental measurement of L_c as $L_c = -\frac{3}{2}\pi\gamma r$. In this way, for our system comprising Si in vacuum, we calculate γ in the range 2.589 to 0.259 J m $^{-2}$ for r from 5 to 50 nm, which compares well to 0.34 J m $^{-2}$ reported in ambient conditions [4] for the tip with radius of curvature $r = 10$ nm. This link allows us to reduce errors that may arise from surface modification leading to change the value of γ . Finally, by substituting this into Eqs. (3) and (2), we obtain

$$a(r, L, L_c) = \left[\frac{3\pi L_c r (1 + \sqrt{1 - L/L_c})^2}{2K} \right]^{\frac{1}{3}}, \quad (4)$$

where the only unknown not derived from the experiment is tip radius of curvature r . The derived radius of the contact, a , that depends on the contact load, L , governs both the thermal conductance of the junction as well as the shear forces, and we will discuss the relevant relationships below.

With single asperity geometry of a tip contact with a planar sample, it is generally accepted that, in vacuum, maximal shear force [33,34] in the junction, F_{ms} , is given by a continuum model such that

$$F_{ms} = \tau\pi a^2, \quad (5)$$

where τ is the constant interfacial shear strength [20,35] and $\pi a^2 = A$ is the contact area between the probe and sample. It should be noted, however, that while this is a most widely accepted approximation, its validity at the nanoscale is still a subject of some debate [36,37]. The thermal resistance of this junction can then, in this general case, be calculated using the method outlined by Prasher [38], that uses the Knudsen number $Kn = \Lambda/a$, where Λ is the mean free path of phonons in the material and a is the characteristic dimension, allowing us to consider both the diffusive ($a \gg \Lambda$) and ballistic ($a < \Lambda$) cases in a single model. According to [38] the thermal resistance of the junction R_j in vacuum can be written as $R_j = \frac{1}{2}ka \left[1 + \frac{8}{3\pi}Kn \right]$ with G_j then determined as

$$G_j = \frac{1}{2ka \left[1 + \frac{8}{3\pi}Kn \right]}, \quad (6)$$

where material thermal conductivity $k = \frac{1}{3}Cv_g\Lambda$, with C being the specific heat capacity per unit volume and v_g the weighted average of the transverse and acoustic phonon group velocities (here we use $C = 1.66 \times 10^6$ J m $^{-3}$ K $^{-1}$ and $v_g = 6400$ m/s for Si) [39,40]. This formula does not account for the interfacial (Kapitza) thermal resistance that can be not insignificant in cases of dissimilar materials [41–43]. At the same time in our case it is a reasonable approximation as two identical materials (Si tip on Si substrate) are used. For thermal resistance lets us consider two boundary cases: the purely diffusive approximation with $Kn \rightarrow 0$ and a ballistic approximation with $Kn \rightarrow \infty$. For the diffusive regime, the junction thermal resistance becomes

$$G_{jd} = 2ka \propto a, \quad (7a)$$

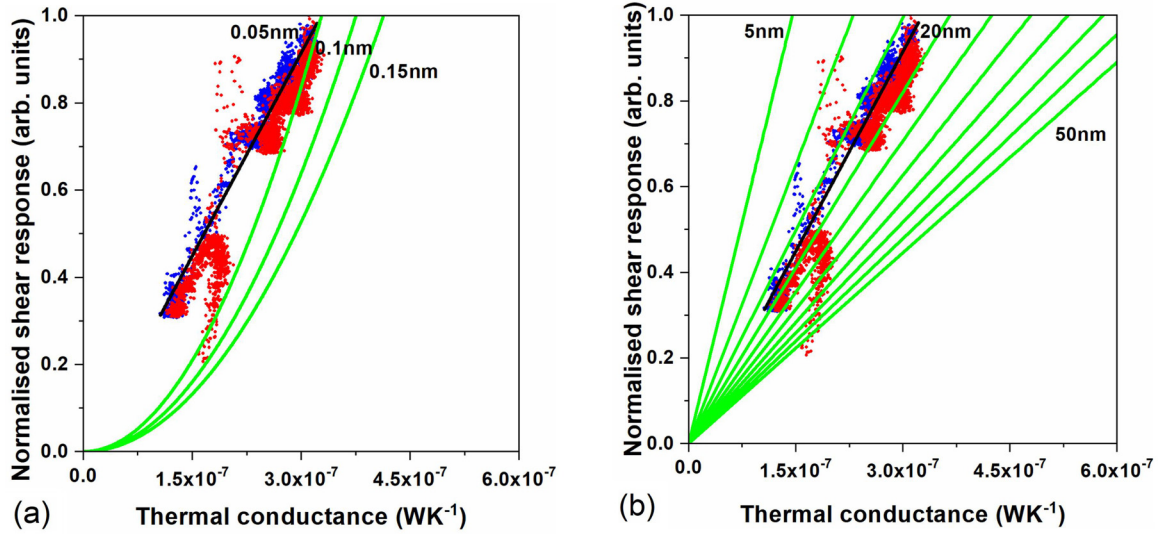


FIG. 2. Comparison of experimentally measured values of normalized maximal shear force $F_{\text{ms-norm}}$ in the junction and junction heat conductance $G_j = 1/R_j$ for approach (blue) and retract (red) data with the model (green) of single asperity contacts in the (a) diffusive (R_{jd}) and (b) ballistic (R_{jb}) approximations. Experimental data are taken from the curves in Fig. 1. The black line is a linear fit to the average of the experimental data, green lines show the modeling data for a series of single asperity contacts incremented in the range of $r = 0.05, 0.1, 0.15$ nm for R_{jd} derived from the diffusive model and $r = 5-50$ nm for R_{jb} from the ballistic models.

whereas for the ballistic heat flow regime the junction resistance is

$$G_{jb} = \frac{3k}{4\Lambda} \pi a^2 = \frac{Cv_g}{4} \pi a^2 \propto a^2 \quad (7b)$$

with a notably different power-law dependence of the contact radius. It would be ideal to plot the dependence of G_{jb} and F_{ms} on the contact radius a , for both these models, and to observe which model fits the experiment. Unfortunately, as the contact radius a is not directly measured in the experiment, we use experimentally measured varied load L as a parameter that changes a according Eq. (4). Also, while values of k and Λ in the Eqs. (7a) and (7b) are known, the value of the shear strength τ in Eq. (5) is generally unknown (see SM for its estimates [22,44]); this value may also change between the different approach: retract curves. Here we eliminated the need to find the absolute values of the shear strength τ , by normalizing the shear force response F_{ms} to 1 for the maximum shear force $F_{\text{ms-max}}$ obtained during each measurement at the same maximum load used in the experiment of $L_{\text{max}} = 200$ nN, with zero corresponding to zero shear force. The normalized shear force response $F_{\text{ms-norm}} = F_{\text{ms}}/F_{\text{ms-norm}}$ can be expressed using Eqs. (4) and (5) as

$$F_{\text{ms-norm}} = \frac{\tau \pi a(r, L, L_c)^2}{\tau \pi a(r, L_{\text{max}}, L_c)^2} = \left(\frac{1 + \sqrt{1 - L/L_c}}{1 + \sqrt{1 - L_{\text{max}}/L_c}} \right)^{3/2}. \quad (8)$$

Using this normalization also allows us to eliminate effect of variability of τ on the $F_{\text{ms-norm}}$ between consecutive experiments. We note that the normalized shear force $F_{\text{ms-norm}}$ would not depend on the radius of curvature of the tip, whereas G_{jb} or G_{jd} will depend on it via $a(r, L, L_c)$. In order to compare the experiment with these models, we substitute the contact radius $a(r, L, L_c)$ obtained from Eq. (4) into

Eq. (7a) (diffusive model) or (7b) (ballistic model) for the thermal conductance, and plot the model and experimentally measured normalized shear force $F_{\text{ms-norm}}$ vs thermal conductance G_j for varying values of load L and various radii of curvature of the tip r . The approach-retract lines in Fig. 1 are discretized and processed into set of data points of varied load [from Fig. 1(b)], absolute thermal conductance using Eq. (1) [from Figs. 1(c) and 1(d)], and normalized shear force $F_{\text{ms-norm}}$ [from Figs. 1(c) and 1(d)], as explained above. It should be noted that the retract data, while confirming the trend, reveal more variability (red curves in Fig. 1), likely due to less stability of the contact. Here we include experimental responses for both probe approach and retraction for positive loads ($L > 0$ nN) to avoid additional instability of the tip-surface contact at negative loads.

By assuming the diffusive heat transport approximation according to Eq. (7a) [Fig. 2(a)], the model cannot provide a reasonable fit to the experimental data for any single value of the tip radius of curvature r : straddling requires values of r that are a factor of 3 different for the loads involved. The absence of the fit for the varying load, and, even more significantly, the fact that the model requires physically unrealistic radii of curvature below 100 pm, suggests that a diffusive model cannot reliably describe the junction contact in this experiment. At the same time, the ballistic approximation described in Eq. (7b) produces a high quality fit for a single value of contact radius r between 15 and 20 nm, which matches well the manufacturers stated value of $r < 30$ nm, which is not observed to change appreciably after many (~ 100) measurements, with excellent fit for the measured range of data for shear strength and the thermal conductance. This reflects the fact that both G_{jb} in the ballistic regime and F_{ms} are directly proportional to the *actual* contact area $A = \pi a^2$ between the probe and sample, as seen in Eqs. (5) and (7b). It can be noted that the interfacial thermal resistance

may produce similar dependence, as it also scales linearly with the contact area. We believe that this cannot dominate the observed effects due to the two identical materials (Si-Si) involved in the contact. In order to rule out the effect of the oxide layer that would present additional thermal resistance, we performed control experiments (see SM note on effect of native oxide) by HF etching of the oxide and comparing the resulting thermal conductance with a nonetched sample. We found that oxide would produce up to 25% increase of the thermal resistance. Given that the observed change in the thermal conductance as in Fig. 2 was 300%, we conclude that junction thermal resistance is principally governed by the mechanisms described above. At the same time, while the proposed explanation of ballistic thermal transport in the junction is most likely correct, such consideration may affect other contact pairs, and would need more detailed studies using differing materials.

It should also be noted that the JKR model suggests the finite minimal stable contact area, whereas in the other often used contact mechanics model, Derjaguin-Muller-Toporov (DMT), the minimal contact area is zero [45–47]. As we see from Figs. 1(c) and 1(d), there is a clear “jump” for both thermal conductance and the shear force, suggesting finite contact area and therefore favoring the JKR model. At the same time, DMT contact mechanics and ballistic thermal transport model (see SM for comparison of the DMT model for various r and L [22]) also shows good quality fit at similar radii around 15–20 nm, indicating that for the positive loads used in experiments both JKR and DMT adhesion models are sufficiently close. Nevertheless, essentially, for both JKR and DMT models the diffusive thermal transport approximation requires unrealistically small contact radii, as stated above. We note that the experimental ratio in Fig. 2 (black line), while generally linear, has some scatter and branching, suggesting that the probe contact radius may have varied during the measurement cycle, e.g., between measurement of adhesion and the thermal and shear response. These details may be further investigated using a more detailed contact model using, for example, molecular dynamic simulations [37].

This study essentially links two dissimilar physical entities—mechanical forces in the contact and the thermal transport—allowing us to relate the thermal conductance G_j with the normalized shear force F_{ms}/τ in a nanoscale contact between the same material via the fundamental parameters of group velocity and heat capacity:

$$G_j = \frac{Cv_g}{4} \left(\frac{F_{ms}}{\tau} \right). \quad (9)$$

The link between two experimentally measured physical values can be likened to the Wiedemann-Franz law [16] describing the relationship between the thermal and electrical con-

ductivity of a metal via charge carriers [48], although in our case the linking element is not the charge or heat carriers but the dimensions of the nanoscale contact area through which both force and thermal interactions occur via fundamental materials properties such as heat capacity and phonon group velocity. Crucially, as the nanoscale junction operates in the ballistic limit of thermal transport, the MFP of phonons need not be considered. This equation is valid when average group velocity for phonon modes [49] remains a good approximation and the phonon wavelength is smaller than the contact dimensions that for typical solid would mean temperatures above 50 K. In the case of different contacting materials ($i = 1, 2$), as the force and shear strength are common for each pair, and the resistance of the probe and the sample are connected in series [9,12], one would expect the parameters of heterogeneous contact [50] to be replaced with the harmonic average value $(Cv_g)_{het} = \frac{2C_1C_2v_{g1}v_{g2}}{C_1v_{g1} + C_2v_{g2}}$ of contacting materials. As we confirmed that it is the total area that governs both heat transport and shear forces, this relation becomes valid for a generic multiasperity contacts with heat transport depending on the total area rather than the linear dimension of the elemental contact.

In conclusion, we elucidate heat transport in nanoscale solid-solid contacts by simultaneous monitoring of shear forces and the heat transport in the scanning thermal microscopy approach. We observed a clear correlation between the thermal conductance and the maximal shear forces in the junction as normal load was varied when establishing and breaking nanoscale contact. The dimensional dependence of the measurements suggests that the heat transport in these typical nanoscale solid-solid contacts is likely to be ballistic in nature. Furthermore, we were able to propose a generalized relationship between a continuum model of shear response and thermal conductance for nanoscale contacts, which describes practically any nanoscale contact pairs having phonon dominated heat transport and may play a significant role in improving the quality and reliability of measurements of nanoscale thermophysical properties and development of nanoelectromechanical systems.

ACKNOWLEDGMENTS

We thank Peter Tovee for help with the SThM instrumentation, Jean Spiece and Charalambos Evangelis for measurements of oxide stripped Si samples, and Vladimir Fal’ko for useful discussions. The authors are also grateful for funding by the EU (Projects FUNPROB, EU FP7 project PIRSES-GA-2010-269169, and QUANTIHEAT, EU FP7 project under grant agreement 604668), by the UK EPSRC, (Grants No. EP/K023373/1 and No. EP/G015570/1), by an EPSRC feasibility study (Grant No. EP/P006973/1), and by the Paul Instrument Fund, c/o The Royal Society, UK.

[1] S. T. Nikhil and B. Bharat, *Nanotechnology* **15**, 1561 (2004).

[2] G. Pernot, M. Stoffel, I. Savic, F. Pezzoli, P. Chen, G. Savelli, A. Jacquot, J. Schumann, U. Denker, I. Mönch, C. Deneke, O. G. Schmidt, J. M. Rampnoux, S. Wang, M. Plissonnier, A. Rastelli, S. Dilhaire, and N. Mingo, *Nat Mater* **9**, 491 (2010).

[3] C. J. Lambert, *Chem. Soc. Rev.* **44**, 875 (2015).

[4] B. J. Robinson and O. V. Kolosov, *Nanoscale* **6**, 10806 (2014).

[5] E. Pop, *Nano Res.* **3**, 147 (2010).

[6] K. M. Hoogeboom-Pot, J. N. Hernandez-Charpak, X. Gu, T. D. Frazer, E. H. Anderson, W. Chao, R. W. Falcone, R. Yang, M. M. Murnane, H. C. Kapteyn, and D. Nardi, *Proc. Natl. Acad. Sci. USA* **112**, 4846 (2015).

- [7] J. A. Johnson, A. A. Maznev, J. Cuffe, J. K. Eliason, A. J. Minnich, T. Kehoe, C. M. S. Torres, G. Chen, and K. A. Nelson, *Phys. Rev. Lett.* **110**, 025901 (2013).
- [8] S. Gomès, A. Assy, and P.-O. Chapuis, *Phys. Status Solidi A* **212**, 477 (2015).
- [9] L. Shi and A. Majumdar, *J. Heat Transfer* **124**, 329 (2002).
- [10] K. Kim, W. Jeong, W. Lee, S. Sadat, D. Thompson, E. Meyhofer, and P. Reddy, *Appl. Phys. Lett.* **105**, 203107 (2014).
- [11] M. Hinz, O. Marti, B. Gotsmann, M. A. Lantz, and U. Durig, *Appl. Phys. Lett.* **92**, 043122 (2008).
- [12] M. E. Pumarol, M. C. Rosamond, P. Tovee, M. C. Petty, D. A. Zeze, V. Falko, and O. V. Kolosov, *Nano Lett.* **12**, 2906 (2012).
- [13] L. Cui, W. Jeong, S. Hur, M. Matt, J. C. Klöckner, F. Pauly, P. Nielaba, J. C. Cuevas, E. Meyhofer, and P. Reddy, *Science* **355**, 1192 (2017).
- [14] N. Mosso, U. Drechsler, F. Menges, P. Nirmalraj, S. Karg, H. Riel, and B. Gotsmann, *Nat Nano* **12**, 430 (2017).
- [15] D. G. Cahill, P. V. Braun, G. Chen, D. R. Clarke, S. Fan, K. E. Goodson, P. Keblinski, W. P. King, G. D. Mahan, A. Majumdar, H. J. Maris, S. R. Phillpot, E. Pop, and L. Shi, *Appl. Phys. Rev.* **1**, 011305 (2014).
- [16] R. Franz and G. Wiedemann, *Ann. Phys. (NY)* **165**, 497 (1853).
- [17] B. Gotsmann and M. A. Lantz, *Nat Mater* **12**, 59 (2013).
- [18] L.-Y. Lin, D.-E. Kim, W.-K. Kim, and S.-C. Jun, *Surf. Coat. Technol.* **205**, 4864 (2011).
- [19] B. J. Robinson, N. D. Kay, and O. V. Kolosov, *Langmuir* **29**, 7735 (2013).
- [20] R. W. Carpick and M. Salmeron, *Chem. Rev.* **97**, 1163 (1997).
- [21] B. Bhushan, *Wear* **259**, 1507 (2005).
- [22] See Supplemental Material at <http://link.aps.org/supplemental/10.1103/PhysRevB.100.235426> for details of experimental methods, correlation analysis, and further details of JKR and DMT contact analysis.
- [23] P. Tovee, M. E. Pumarol, D. A. Zeze, K. Kjoller, and O. Kolosov, *J. Appl. Phys.* **112**, 114317 (2012).
- [24] A. Majumdar, *Annu. Rev. Mater. Sci.* **29**, 505 (1999).
- [25] P. D. Tovee and O. V. Kolosov, *Nanotechnology* **24**, 465706 (2013).
- [26] H.-J. Butt, B. Cappella, and M. Kappl, *Surf. Sci. Rep.* **59**, 1 (2005).
- [27] D. G. Cahill, W. K. Ford, K. E. Goodson, G. D. Mahan, A. Majumdar, H. J. Maris, R. Merlin, and S. R. Phillpot, *J. Appl. Phys.* **93**, 793 (2003).
- [28] S. Lefèvre, S. Volz, and P.-O. Chapuis, *Int. J. Heat Mass Transfer* **49**, 251 (2006).
- [29] K. Luo, Z. Shi, J. Varesi, and A. Majumdar, *J. Vac. Sci. Technol. B* **15**, 349 (1997).
- [30] R. W. Carpick, N. Agrait, D. F. Ogletree, and M. Salmeron, *Langmuir* **12**, 3334 (1996).
- [31] R. W. Carpick, D. F. Ogletree, and M. Salmeron, *J. Colloid Interface Sci.* **211**, 395 (1999).
- [32] O. V. Kolosov, M. R. Castell, C. D. Marsh, G. A. D. Briggs, T. I. Kamins, and R. S. Williams, *Phys. Rev. Lett.* **81**, 1046 (1998).
- [33] U. D. Schwarz, O. Zworner, P. Koster, and R. Wiesendanger, *Phys. Rev. B* **56**, 6987 (1997).
- [34] S. Franzka and K. H. Zum Gahr, *Tribol. Lett.* **2**, 207 (1996).
- [35] M. Daly, C. Cao, H. Sun, Y. Sun, T. Filleter, and C. V. Singh, *ACS Nano* **10**, 1939 (2016).
- [36] J. Gao, W. D. Luedtke, D. Gourdon, M. Ruths, J. N. Israelachvili, and U. Landman, *J. Phys. Chem. B* **108**, 3410 (2004).
- [37] Y. Mo, K. T. Turner, and I. Szlufarska, *Nature (London)* **457**, 1116 (2009).
- [38] R. Prasher, *Nano Lett.* **5**, 2155 (2005).
- [39] G. Chen, *Phys. Rev. B: Condens. Matter Mater. Phys.* **57**, 14958 (1998).
- [40] M. G. Holland, *Phys. Rev.* **132**, 2461 (1963).
- [41] N. Maxim, C. R. Mark, J. G. Andrew, V. K. Oleg, G. D. Vladimir, and A. Z. Dagou, *J. Phys. D Appl. Phys.* **50**, 494004 (2017).
- [42] B. Deng, A. Chernatynskiy, M. Khafizov, D. H. Hurley, and S. R. Phillpot, *J. Appl. Phys.* **115**, 084910 (2014).
- [43] G. Balasubramanian and I. K. Puri, *Appl. Phys. Lett.* **99**, 013116 (2011).
- [44] Z. Deng, N. N. Klimov, S. D. Solares, T. Li, H. Xu, and R. J. Cannara, *Langmuir* **29**, 235 (2013).
- [45] D. Maugis, *J. Colloid Interface Sci.* **150**, 243 (1992).
- [46] K. L. Johnson, *Langmuir* **12**, 4510 (1996).
- [47] V. M. Muller, V. S. Yushchenko, and B. V. Derjaguin, *J. Colloid Interface Sci.* **77**, 91 (1980).
- [48] R. B. Wilson and D. G. Cahill, *Phys. Rev. Lett.* **108**, 255901 (2012).
- [49] A. S. Henry and G. Chen, *J. Comput. Theor. Nanosci.* **5**, 141 (2008).
- [50] T. Miloh and Y. Benveniste, *Proc. R. Soc. A* **455**, 2687 (1999).